Supplementary Information:

Microscale investigation on interfacial slippage and detachment of ice from soft materials

Kartik Regulagadda[a,†], Julia Gerber[a,†], Thomas M. Schutzius[b,1], Dimos Poulikakos[a,2]

[a]Laboratory of Thermodynamics in Emerging Technologies, Department of Mechanical and Process Engineering, ETH Zurich, Sonneggstrasse 3, CH-8092 Zurich, Switzerland

[b]Laboratory for Multiphase Thermofluidics and Surface Nanoengineering, Department of Mechanical and Process Engineering, ETH Zurich, Sonneggstrasse 3, CH-8092 Zurich, Switzerland

† Equally contributing authors

[1] To whom correspondence should be addressed: Prof. Thomas M. Schutzius, ETH Zurich, Laboratory for Mulitphase Thermofluidics and Surface Nanoengineering, Sonneggstrasse 3, ML J 27.2, CH-8092 Zurich, Switzerland; Phone: +41 44 632 46 04; E-mail: thomschu@ethz.ch

[2] To whom correspondence should be addressed: Prof. Dimos Poulikakos, ETH Zurich, Laboratory of Thermodynamics in Emerging Technologies, Sonneggstrasse 3, ML J 36, CH-8092 Zurich, Switzerland. Phone: +41 44 632 27 38; Fax: +41 44 632 11 76; E-mail: dpoulikakos@ethz.ch;

Table of contens

Section S1. Materials

We used Silicone CY 52-276 from Dow Corning for fabricating the soft surfaces. Poly (dimethylsiloxane-b-ethylene) oxide (or simply PEO) from Polysciences is mixed with the elastomer in cTFM experiments. Circular (diameter 24 mm, thickness 0.17 mm) and rectangular (26 x 20 mm, thickness 0.4 mm) glass cover slips from Roth AG are used either as purchased or cleaned, and activated in Oxygen plasma (10 min, 100 W; Plasma Asher Diener). The other substrates are PMMA discs (diameter 24 mm, thickness 1 mm), microscope slides (76 x 26 mm, thickness 1 mm) from VWR international cut into rectangular shape (25 x 26 mm), and copper samples (20 x 20 mm, thickness 1 mm). For cleaning the substrates, we employed Acetone, Isopropyl alcohol (IPA), and 1M Hydrochloric acid procured from Sigma Aldrich, and de-ionized (DI) water. For oil infused polymer networks, silicon fluid (Xiameter PMX-200/100 cs) was utilised.

Section S2. Soft substrate preparation and QD printing method

The two components of Silicone CY 52-276, A and B are mixed in w/w ratio of 5:6 for 5 min. The mixture is degassed for 3 min and spin coated on untreated glass cover slips at 800, 1500, and 5000 rpm (to vary the thickness, h) for 1 min. The samples are cured in an oven at 70 °C for 30 min. For the oil infused soft surfaces, we add 20% silicon fluid by weight after mixing A and B components, and follow a similar protocol. For the bright field microscopy, the cut and cleaned microscope slides are spin coated at 1500 rpm following a similar protocol. For experiments with cTFM, we added 0.05% v/v PEO to the elastomer components before mixing. With the rest of the protocol being the same, the rectangular coverslips are spin coated at 1500 rpm. Once the QD printing is complete, we bake the sample in a vacuum chamber at 90 °C for 1 hour followed by Methanol washing for 2 min and again baking in the vacuum chamber for 2 hours. To fabricate samples with ultrathin layer of elastomer, we dissolved the elastomer solution in toluene with a w/v ratio of 5%, and vortexed continuously for 12 hours. The solution is spin coated on plasma treated cover slips at 5000 rpm for 1 min. The coated samples are cured in an oven at 90 °C for 1 hour to make sure that the solvent evaporates completely. The thickness of the elastomer layer on the samples is measured using a laser-scanning microscope (Keyence VKX-100) except for the toluene dissolved samples. For the latter, the sample is broken at the center after it is plunged into liquid Nitrogen, and the cross-section is imaged in SEM (Hitachi SU8230) to obtain the layer thickness.

The samples used for traction force microscopy measurements were subsequently treated in the following way. The QDs were printed onto the substrate by electrohydrodynamic NanoDrip-printing, as reported previously[1–5]. After placing the substrate on a conducting grounded plate, a gold-coated glass capillary with an opening diameter of 1−1.5 μm is filled with a colloidal QD

solution. Then the capillary is approached towards the substrate using a piezoelectric stage until reaching a distance of 5-10 μm. Applying voltage pulses between the nozzle and the grounded plate leads to the formation of an apex at a larger meniscus at the nozzle exit. From this apex, nanoscale droplets with a diameter of 150–250 nm are ejected with frequencies of 100–200 Hz. After evaporation of the solvent, the nanoparticle content is left behind in a narrow footprint, because there is no splashing or sizable spreading at droplet landing. DC voltages of 240-260 V are applied for 120 ms, resulting in the deposition of multiple nanodroplets at the same location, thus collectively forming one brightly emitting disc at a well-defined position, which we term a nanodisc. Arbitrary patterns can be created moving the substrate with a piezoelectric stage, but here a triangular mesh was selected. The red core–shell–shell CdSe–CdS–ZnS QDs with an emission peak at 627 nm were synthesized following a published recipe.[4]

For the substrates used in the material characterization at low temperature, we drop casted ≈1 mm thick layer of the elastomer mixture on a cleaned copper substrate. The samples are cured in an oven at 70 °C for 30 min. The copper substrate is cleaned with DI water, Acetone, IPA for 10 min each in that order in a sonication bath. This is followed by sonication in 1M HCl for 10 min. Finally, the substrate is rinsed in DI water and dried with Nitrogen at ambient temperature, T_{amb} = 21 °C.

Section S3. Displacement tracking and Ogden model

The QDs are tracked using a commercially available software (Imaris 9.2.1) in each time step. The coordinates of QDs spotted at time, $t = 0$ are taken as the reference configuration. Even in the reference state, not all the printed QDs are detected owing to non-uniform illumination from the laser. We apply the local normalization filter to the images using a freeware (ImageJ 1.52p) to address this issue to some extent. For the displacement, $U_{x,i}$, of each particle, we manually track QDs using a freeware (ImageJ 1.52p). In each time step, using an affine transformation we correlate the current and the reference configuration co-ordinates to find the principal stretches, λ_i (i = 1, 2, and 3), of the elastomer as described in Ref.[6] We then estimate the 2nd order Ogden strain-energy function, W, with the material constants shown in Table 1.

Table S1| Ogden material parameters for Si CY 52-276 A:B 5:6

μ_1 (kPa)	μ_2 (kPa)	α_1 (-)	α_2 (-)
6.055	0.313×10^{-3}	1.607	-5.885

These constants are obtained by fitting the experimental data of uniaxial and biaxial tests provided in Ref.[1] into the 2nd order Ogden model using a commercial software (Abaqus CAE 6.14). This model is found to be a good fit considering the strain ranges in the cTFM experiments reported in previous work.[1,2,5] Additionally, this model fits the experimental uniaxial and biaxial test data—obtained in a previous study[1]— better compared to the other common hyperelastic models for elastomer behavior like the Neo-Hookean, Mooney-Rivlin, and Yeoh models (see Supplementary Fig. S11). Although the reported data is at ambient temperature, $T_{amb} = 21$ ºC, we assume that it is valid even at $T = -20$ ºC since the variation of Young's modulus is below 25% (see Fig. 3a). The

principal stresses, ξ_i (i = 1, 2, and 3), are estimated as $\xi_i = \lambda_i \frac{\partial W}{\partial \lambda_i} - p$ where p is the hydrostatic stress. Assuming that the pure shear boundary condition is valid i.e. $\xi_3 = 0$, we estimate the remaining principal stresses. The absolute maximum of these two stresses is considered as the Ogden shear stress, τ_{Ogden}, for each time step. For $V = 0.1$ mm/s, since few QDs are tracked, any local behavior will get amplified leading to an error in τ_{Ogden}. Therefore, we estimate τ_{Ogden} only until a point where there are no numerical artifacts. Further, as we cannot reduce the exposure time below 0.1 s to capture QDs with sufficient intensity, experiments with V > 0.1 mm/s are not feasible as we observe streaks rather than dots. We also had data spooling issues at an fps > 5. Thus, we restricted the cTFM measurements to $V \leq 0.1$ mm/s.

Section S4. Low-temperature material characterization

A thick film coated copper substrate is cooled down to the desired temperature using the cryostage. The entire experiment is again carried out in a chamber with Nitrogen supply so that the relative humidity, RH < 10%. A femto-tool (FemtoTools AG Micromechanical Testing Station FT-MTA02) is used to indent the elastomer at a speed of 2 μm/s. The femto-tool is essentially a force gauge capable of precise measurements in the order of ≈1 μN. The tip of the tool is customized to have a smooth sphere with a radius, r = 100 μm. The maximum indentation depth, $\delta_{max} < 0.1r$ so that Hertz theory of sphere contacting an infinite medium can be applied. The Poisson's ratio, ϑ, of the elastomer is assumed to be 0.5 i.e. incompressible material. The femto-tool software gives the plot of force, F, vs displacement, θ. From Hertz's theory,[7] we estimate the Young's modulus, $E = 3\alpha(1-\vartheta^2)/(4r^{0.5})$ where α is a fitting parameter obtained by fitting the force function $F = \alpha\theta^{1.5}$ using Nelder-Mead downhill simplex algorithm in Python. The method is extremely sensitive to aspects like frost formation on the elastomer, Nitrogen flow in the chamber, and even cold Nitrogen flow in the cryostage. Frost formation affects the indentation process leading to over estimation of the modulus. The Nitrogen flow in the chamber or the cryostage induces noise in the femto-tool measurements as the sensitivity is quite high. Therefore, supply of Nitrogen to the chamber and liquid Nitrogen to the cryostage are shut down once the desired substrate temperature, T, is attained. This leads to gradual increase of RH, and T. By the time the indentation process is complete, we observed an increase in $T \approx 2$ ºC, and $RH \approx 5\%$. Additionally, frost formation was extremely rapid at $T <$ -20 ºC when supply of Nitrogen to the chamber was cut-off. Therefore, many experiments resulted in erroneous results. Hence, the results of only independent experiments are reported for $T <$ -20 ºC.

Section S5. Supplementary figures

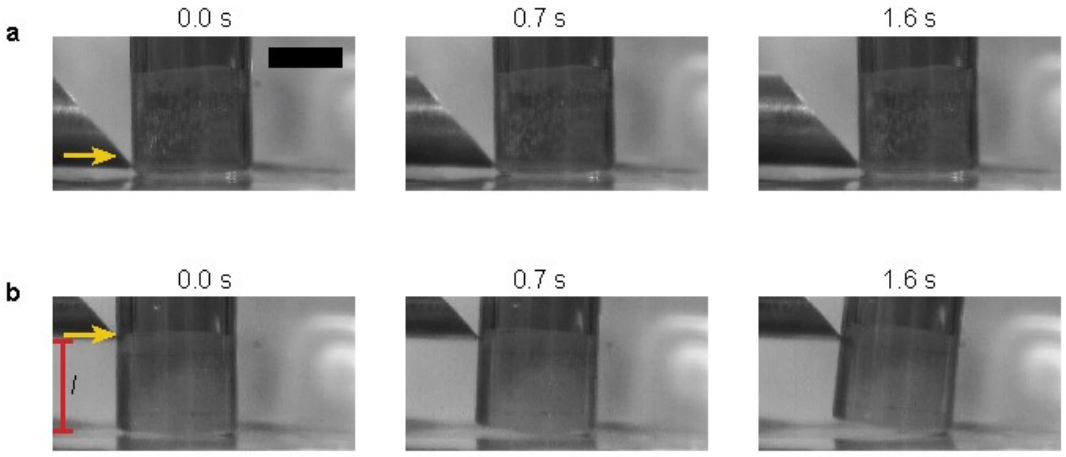

Supplementary Fig. S1 Macroscopic ice adhesion tests: Selected snapshots of ice adhesion tests in shear **(a)**, and mixed **(b)** modes with h = 35 μm, V = 1 mm/s, and T = -20 ºC. Ice continues to slip as long as shear is applied in **(a)**. However, we have interfacial fracture in **(b)** as ice clearly de-bonds from the elastomer. The height at which the force pin contacts the ice block in **(b)**, l = 6.1 mm. Time t = 0 is taken when the force pin contacts the ice block. Scale bar: **a**, 5 mm.

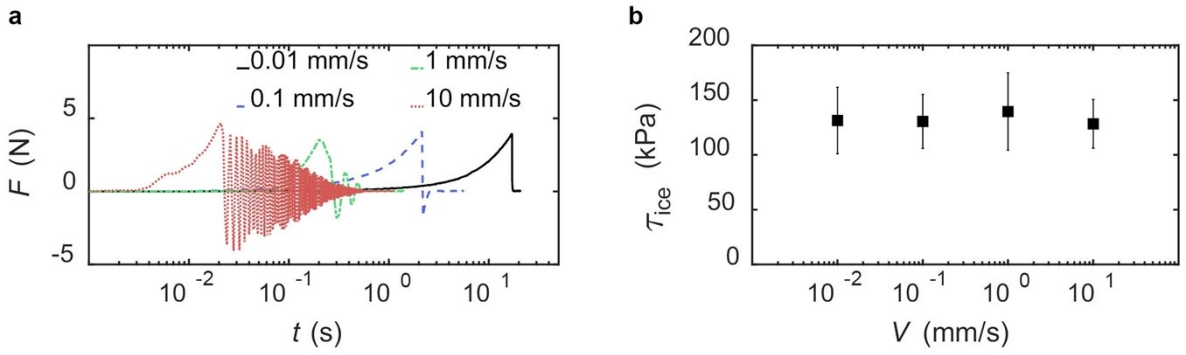

Supplementary Fig. S2 Independency of ice adhesion shear strength on a hard PMMA substrate. a Representative force, F, vs time, t, plots at different force pin velocity, V, on a PMMA substrate at a surface temperature, T = -20 °C in mixed mode test. The peak force is practically independent of V as opposed to the trend observed on elastomers. Time, t = 0 is taken just before the instance when force has non-zero values. **b** Plot showing the independence of ice adhesion shear strength, τ_{ice}, with V at T = -20° C on PMMA in mixed mode test. Error bars represent standard deviation for $n_e \geq 3$ independent experiments.

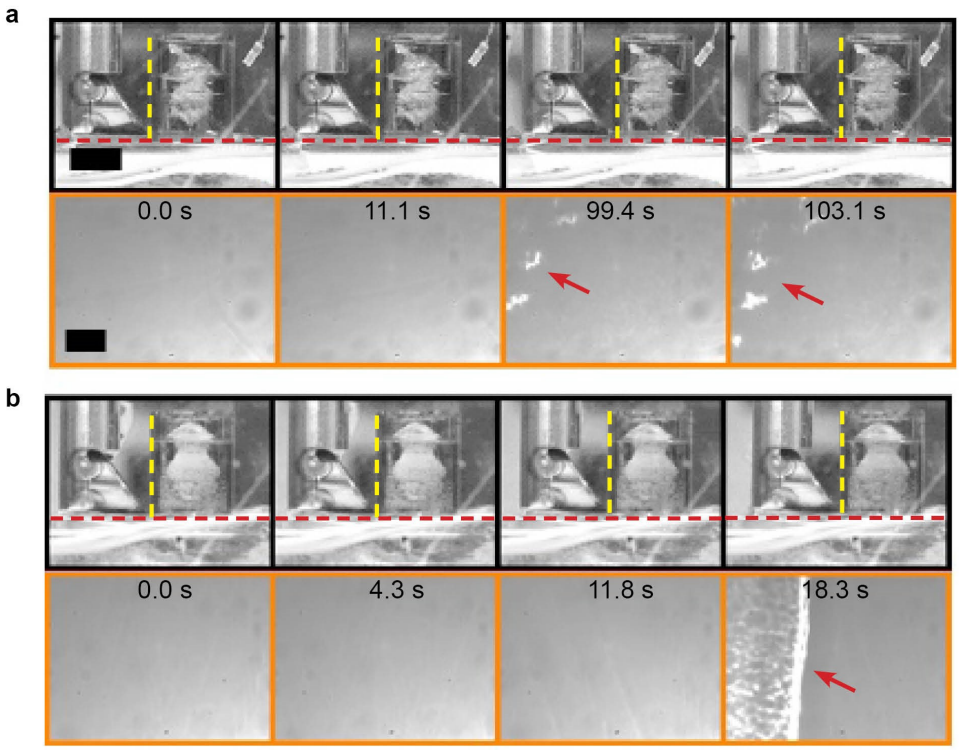

Supplementary Fig. S3 Bright field microscopy at different force pin velocities. a-b Selected snapshots of side and bottom view at a force pin velocity, $V = 0.01$, and 0.1mm/s respectively. Time, $t = 0$ at the instance when the force pin contacts the cuvette. The dashed red and yellow lines in the side view indicate the ice-elastomer interface and the contact position of the force pin with the cuvette, respectively. The red arrows in the bottom view indicate the inner boundary of the cuvette. Clearly, in both the cases, ice block slips on the elastomer as no surface undulations can be observed in the bottom view. The field of view in the bottom view is smaller than the entire ice-elastomer area. Scale bars, **a** (side view) 5 mm, and **a** (bottom view), 0.1 mm.

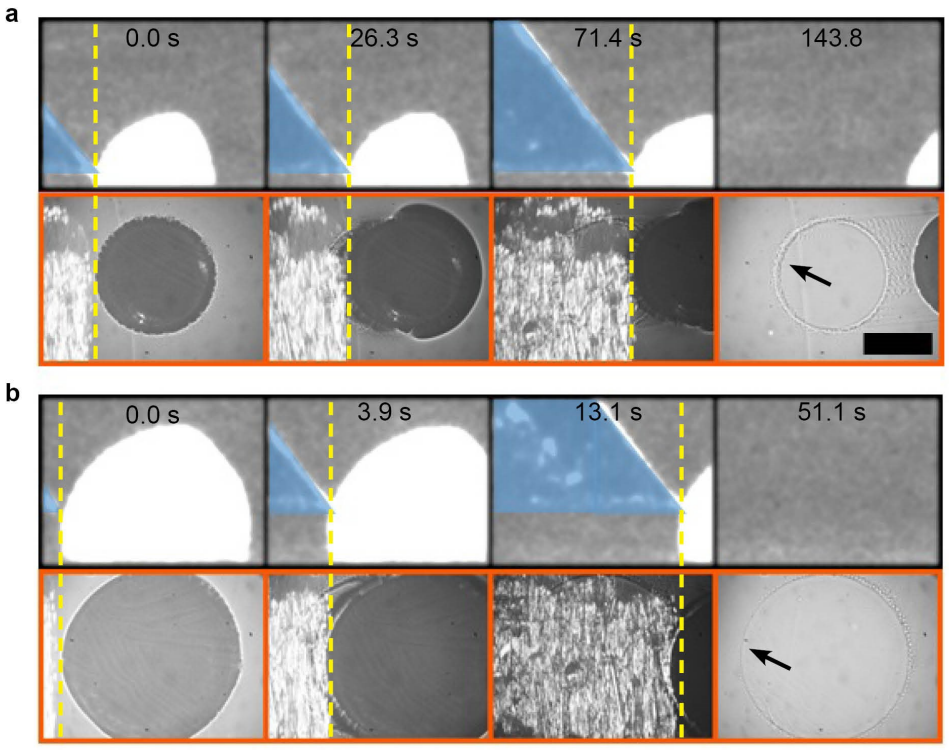

Supplementary Fig. S4 Bright field microscopy of a frozen water droplet at different force pin velocities. a-b Selected snapshots of side and bottom view at a force pin velocity, $V = 0.01$, and 0.1 mm/s respectively. The entire ice-elastomer area can be visualized with this experiment during the adhesion test. The force pin is false colored in blue for clarity. The dashed yellow line in the side view indicates the contact position of the force pin with the ice droplet. Time, $t = 0$ at the instance when the force pin contacts the ice droplet. Again, in both the cases, the ice droplet slips on the elastomer as no surface undulations can be observed. We only observe ring-like structures (black arrows) near the contact line of the initial ice droplet location which could be due to elastic instabilities near the edge during the adhesion test. Scale bar, **a,** 0.5 mm.

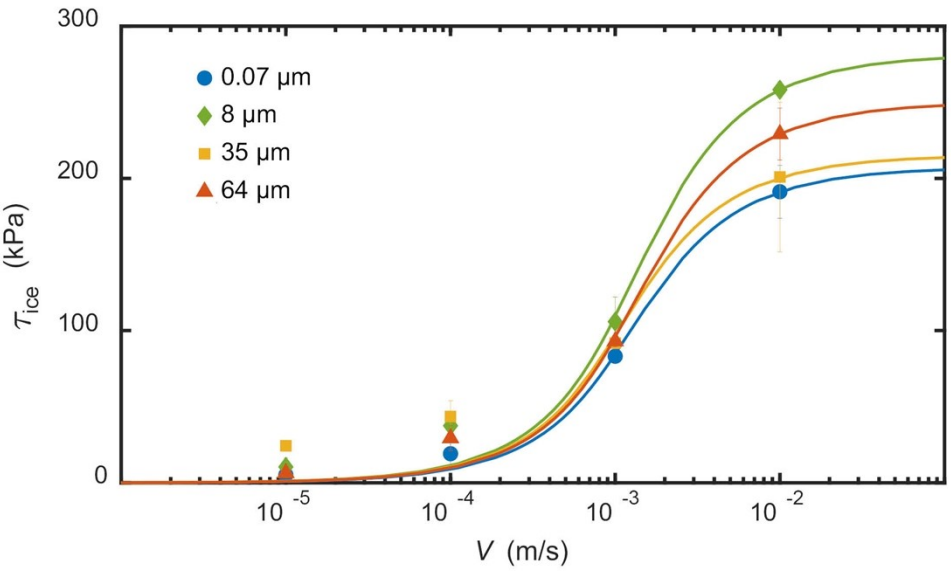

Supplementary Fig. S5. Effect of shear velocity on ice adhesion in shear mode test. Variation of τ_{ice} with shear velocity, V, for different elastomer thickness, h, at an elastomer surface temperature, T = -20 °C. All the data points follow a similar trend as explained in the main text. The solid curves indicate the best fit of Chernyak and Leonov adhesive friction model (Eq. 1 in the main text) to the experimental data. The model parameters a, B, and m are shown in Supplementary Table 1. Error bars represent standard deviation for $n_e \geq 3$ independent experiments.

Supplementary Table 1: Table showing the friction model parameters

Elsatomer Thickness (μm)	***a***	***B* (s/m)**	***m***
0.07	80.74	213.3	5.5×10^{-8}
8	109.6	201.2	5.2×10^{-8}
35	83.83	241	2.3×10^{-8}
64	97.41	197.2	2.5×10^{-8}

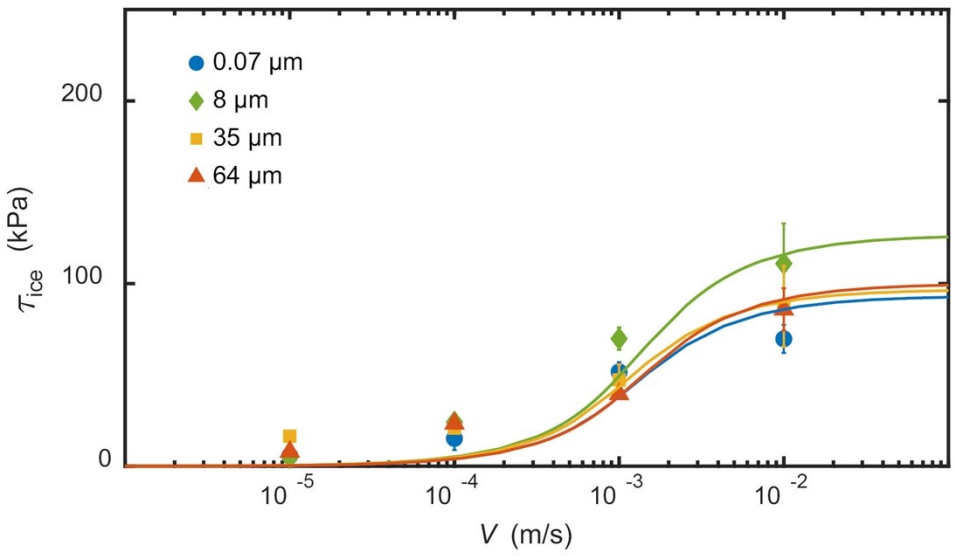

Supplementary Fig. S6. Effect of shear velocity on ice adhesion in mixed mode test. Variation of τ_{ice} with shear velocity, V, for different elastomer thickness, h, at an elastomer surface temperature, T = -20 °C. All the data points follow a similar trend as explained in the main text. The solid curves indicate $0.45\tau_{ice,s}$ where $\tau_{ice,s} = \tau_{friction}$ (using Eq. 1 from the main text) is the ice adhesion strength in the shear mode when all the other experimental conditions are same. For the sake of clarity, σ_{ice} is not included in the plot. Error bars represent standard deviation for $n_e \geq 3$ independent experiments.

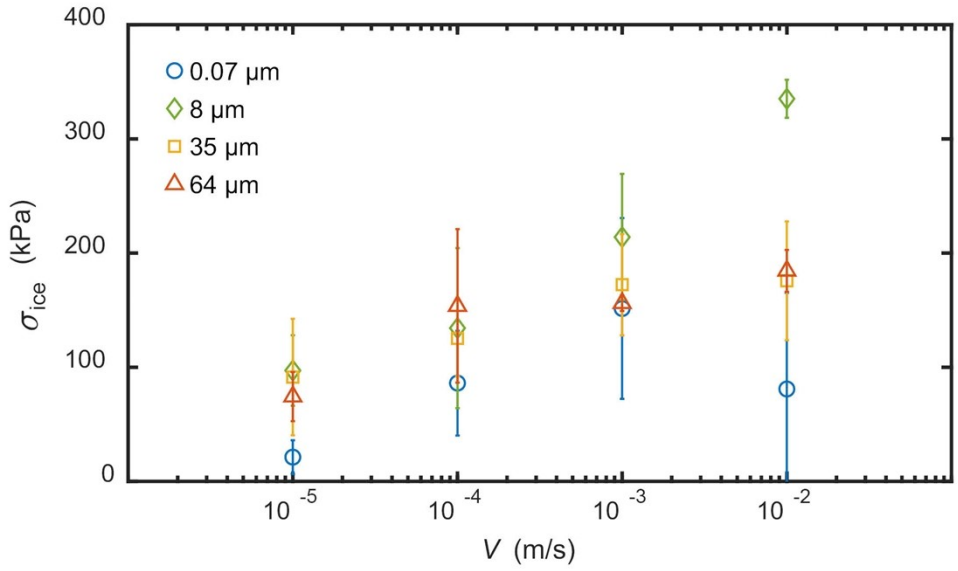

Supplementary Fig. S7. Effect of shear velocity on ice adhesion in normal mode test. Variation of σ_{ice} with shear velocity, V, for different elastomer thickness, h, at an elastomer surface temperature, T = -20 °C. Error bars represent standard deviation for $n_e \geq 3$ independent experiments.

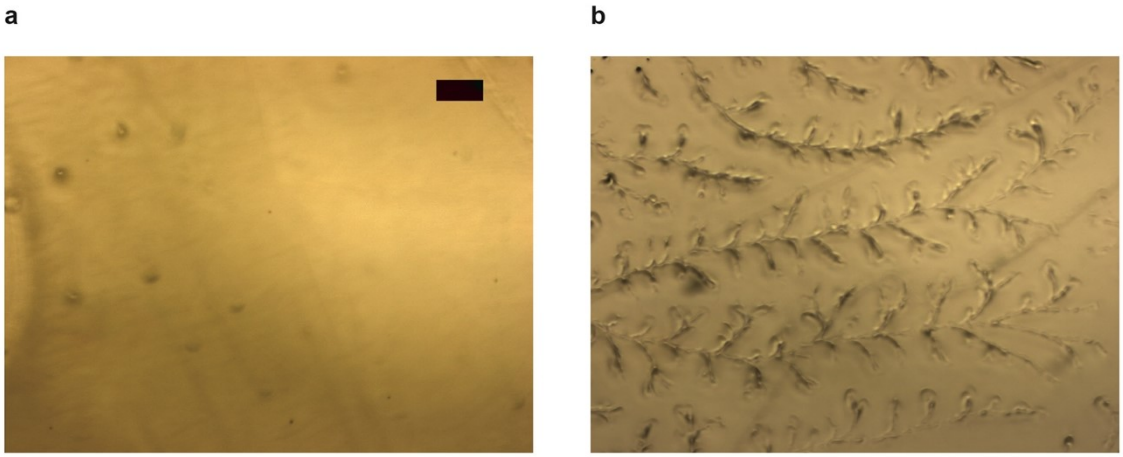

Supplementary Fig. S8. Partial cohesive failure of the elastomer during normal mode test. Microscopic images of the elastomer before (**a**) and after (**b**) the normal mode adhesion test at T = -20 °C, h = 35 μm, and V = 10 mm/s. The patterns in **b** clearly indicate the partial cohesive failure of the elastomer. Scale bar, **a** 200 μm.

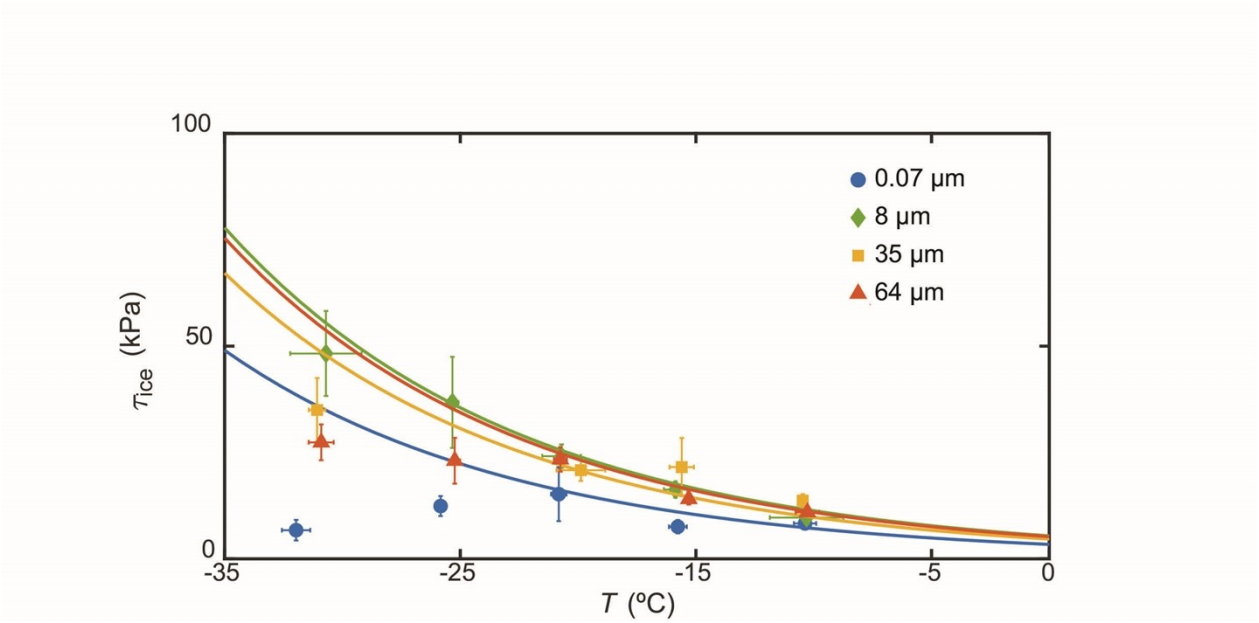

Supplementary Fig. S9. Effect of elastomer temperature on ice adhesion in mixed mode test. Variation of τ_{ice} with elastomer surface temperature, T, at V = 0.1 mm/s for different elastomer thickness, h. The solid curves indicate the Williams-Landel-Ferry transformation to the experimental data. For the sake of clarity, σ_{ice} is not included in the plot. Error bars represent standard deviation for $n_e \geq 3$ independent experiments.

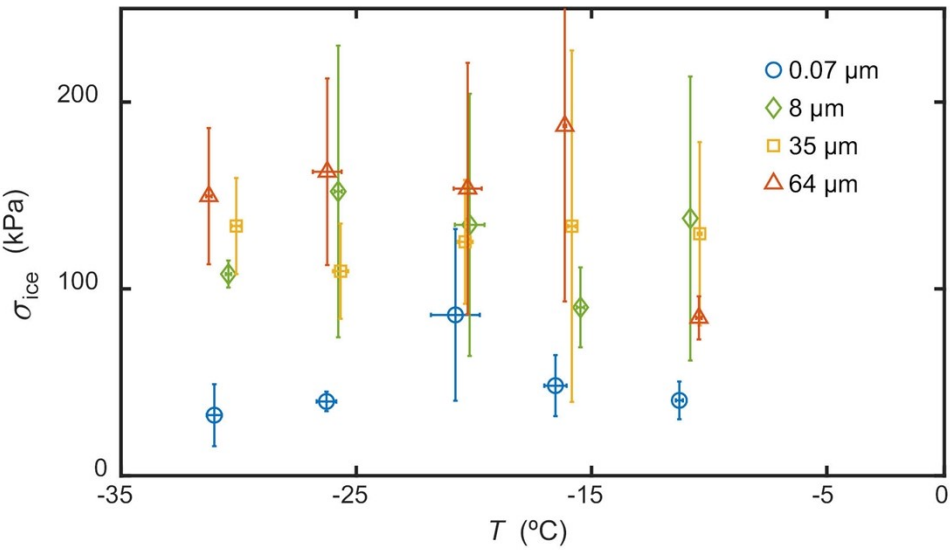

Supplementary Fig. S10. Effect of elastomer temperature on ice adhesion in normal mode test. Variation of σ_{ice} with elastomer surface temperature, T, at V = 0.1 mm/s for different elastomer thickness, h. Error bars represent standard deviation for $n_e \geq 3$ independent experiments.

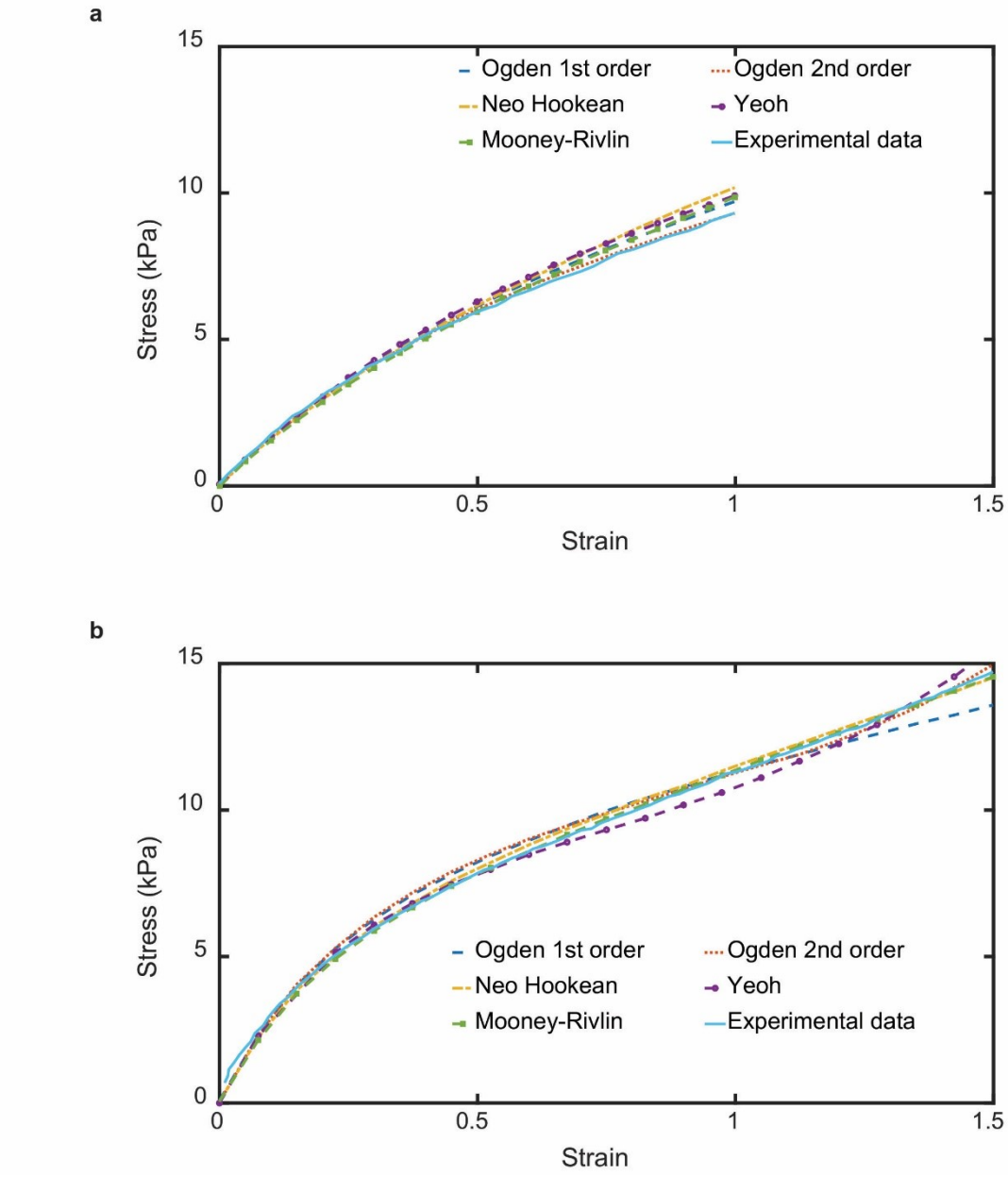

Supplementary Fig. S11. Fit of various hyperelastic models to the uniaxial and biaxial experimental data for Si CY 52-276 A:B 5:6. (a) Plot of stress vs. strain for uniaxial test (b) Plot of stress vs. strain for biaxial test. The Ogden 2nd order model is found to be the best fit considering both the tests which are performed at room temperature (experimental data obtained from Ref.[1]) and therefore is selected for modelling the stress of the elastomer in the ice adhesion test.

Section S6. Supplementary movies description

Supplementary movie S1

Description: Macroscopic shear and mixed mode test. Side view video of shear and mixed mode tests for V = 1 and 10 mm/s at T = -20 °C, and h = 35 μm. Ice slips on the elastomer until V = 1 mm/s in shear mode and de-bonds at V = 10 mm/s while in mixed mode, we have interfacial fracture at all the velocities.

Supplementary movie S2

Description: cTFM experiments. Bottom view video of QD grid to show the response of elastomer as ice is sheared at V = 0.01 mm/s, T = -20 °C, and h = 35 μm.

Supplementary movie S3

Description: cTFM experiments. Bottom view video of QD grid to show the response of elastomer as ice is sheared at V = 0.1 mm/s, T = -20 °C, and h = 35 μm.

Section S7. References

(1) Bergert, M.; Lendenmann, T.; Zündel, M.; Ehret, A. E.; Panozzo, D.; Richner, P.; Kim, D. K.; Kress, S. J. P.; Norris, D. J.; Sorkine-Hornung, O.; Mazza, E.; Poulikakos, D.; Ferrari, A. Confocal Reference Free Traction Force Microscopy. *Nat. Commun.* 2016, **7**, 12814.

(2) Gerber, J.; Lendenmann, T.; Eghlidi, H.; Schutzius, T. M. Wetting Transitions in Droplet Drying on Soft Materials. *Nat. Commun.* 2019, **10**, 4776.

(3) Galliker, P.; Schneider, J.; Eghlidi, H.; Kress, S.; Sandoghdar, V.; Poulikakos, D. Direct Printing of Nanostructures by Electrostatic Autofocussing of Ink Nanodroplets. *Nat. Commun.* 2012, **3**, 1891.

(4) Kress, S. J. P.; Richner, P.; Jayanti, S. V.; Galliker, P.; Kim, D. K.; Poulikakos, D.; Norris, D. J. Near-Field Light Design with Colloidal Quantum Dots for Photonics and Plasmonics. *Nano Lett.* 2014, **14**, 5827–5833.

(5) Lendenmann, T.; Schneider, T.; Dumas, J.; Tarini, M.; Giampietro, C.; Bajpai, A.; Chen, W.; Gerber, J.; Poulikakos, D.; Ferrari, A.; Panozzo, D. Cellogram: On-the-Fly Traction Force Microscopy. *Nano Lett.* 2019, **19**, 6742–6750.

(6) Hopf, R.; Bernardi, L.; Menze, J.; Zündel, M.; Mazza, E.; Ehret, A. E. Experimental and Theoretical Analyses of the Age-Dependent Large-Strain Behavior of Sylgard 184 (10:1) Silicone Elastomer. *J. Mech. Behav. Biomed. Mater.* 2016, **60**, 425–437.

(7) Hertz, H. Ueber Die Berührung Fester Elastischer Körper. *J. fur die Reine und Angew. Math.* 1881, **92**, 156–171.